Low Perfusion Compartments in Glioblastoma Quantified by Advanced Magnetic Resonance Imaging and Correlated with Patient Survival

Chao Li[1,2*], Jiun-Lin Yan[1,3,4], Turid Torheim[5,6], Mary A. McLean[5], Natalie R. Boonzaier[1], Yuan Huang[7,9], Jianmin Yuan[7], Bart RJ Van Dijken[10], Tomasz Matys[7,8], Florian Markowetz[5,6], and Stephen J. Price[1,11]

*Corresponding author: Chao Li; Email: cl109@outlook.com

[1]Brain Tumour Imaging Laboratory, Division of Neurosurgery, Department of Clinical Neuroscience, University of Cambridge, Cambridge, UK;

[2]Department of Neurosurgery, Shanghai General Hospital, Shanghai Jiao Tong University School of Medicine, China (CL);

[3]Department of Neurosurgery, Chang Gung Memorial Hospital, Keelung, Taiwan;

[4]Chang Gung University College of Medicine, Taoyuan, Taiwan;

[5]Cancer Research UK Cambridge Institute, University of Cambridge, Cambridge, UK;

[6]CRUK & EPSRC Cancer Imaging Centre in Cambridge and Manchester, Cambridge, UK;

[7]Department of Radiology, University of Cambridge, Cambridge, UK;

[8]Cancer Trials Unit Department of Oncology, Addenbrooke's Hospital, Cambridge, UK;

[9]EPSRC Centre for Mathematical and Statistical Analysis of Multimodal Clinical Imaging, University of Cambridge, Cambridge, UK;

[10]Department of Radiology, University Medical Center Groningen, University of Groningen, Groningen, the Netherlands.

[11]Wolfson Brain Imaging Centre, Department of Clinical Neuroscience, University of Cambridge, Cambridge, UK;

Abstract

Glioblastoma exhibits profound intratumoral heterogeneity in blood perfusion, which may cause inconsistent therapy response. Particularly, low perfusion may create a hypoxic microenvironment and induce resistant clones. Thus, developing validated imaging approaches that define low perfusion compartments is crucial for clinical management.

Here we present a novel method identifying two low perfusion compartments in glioblastoma using multiparametric physiological magnetic resonance imaging. Both compartments displayed hypoxic and pro-inflammatory metabolic signatures, suggesting selective stress, and affected progression-free survival (PFS) and overall survival (OS). The lactate level in the low perfusion and restricted diffusion compartment showed increased hazard ratio (PFS: HR 2.995, CI 1.012-8.861, P = 0.047; OS: HR 4.974, CI 1.608-15.39, P = 0.005). This compartment may represent a treatment resistant sub-region contributing to glioblastoma invasiveness.

This approach was based on clinically available imaging modalities and could thus provide crucial pretreatment information for clinical decision making.

Introduction

Glioblastoma is a highly aggressive primary tumor in the central nervous system of adults (Weller et al., 2017). Despite advances in treatment, the median overall survival (OS) of glioblastoma patients remains low at 14.6 months (Stupp et al., 2005). Inconsistent response to treatment is a major challenge in glioblastoma treatment stratification and could be caused by the extensive heterogeneity of this disease. Many genetically distinct cancer cell populations can exist in the same tumor and display diverse treatment response (Sottoriva et al., 2013; Verhaak et al., 2010). Developing validated methods to explore intratumoral heterogeneity is crucial for patient subgrouping and personalized treatment.

One of the most fundamental traits of glioblastoma is chronic angiogenesis and elevated perfusion, associated with a more invasive phenotype (Hanahan & Weinberg, 2011; Lathia, Heddleston, Venere, & Rich, 2011). However, a potent angiogenesis inhibitor failed to demonstrate consistent benefits in clinical trials of *de novo* glioblastoma (Chinot et al., 2014). A possible explanation for this failure is the profound intratumor perfusion heterogeneity observed in glioblastomas, which is due to aberrant microvasculature and inefficient nutrient delivery. This heterogeneity can give rise to regions in the tumor where the demand and supply of nutrients is mismatched (Komar et al., 2009). Consequently, the sufficiently perfused sub-regions may hold the advantages for progression and proliferation, whereas the insufficiently perfused sub-regions may have a hypoxic microenvironment (Gillies, Schornack, Secomb, & Raghunand, 1999). The selective stress created thereafter could impact clonal evolution (Quail & Joyce, 2013), and preferentially induce adaptive and treatment resistant clones (Pistollato et al., 2010).

Here we describe a method for identifying low perfusion compartments in glioblastoma using multiparametric physiological magnetic resonance imaging (MRI), which allows a more comprehensive evaluation of tumor physiology compared to the morphological

heterogeneity visualized by structural MRIs. Our approach improves on current clinical practice, which can lead to non-specific results by inferring low perfusion sub-regions as non-enhancing regions within an otherwise contrast enhancing volume on post-contrast T1-weighted structural images (O'Connor et al., 2015).

The two low perfusion compartments we visualized have distinct cellularity: one compartment with increased cellularity representing a population adapted to hypoxic acidic conditions (Gatenby, Grove, & Gillies, 2013), and one compartment with low cellularity representing a necrotic region. By combining perfusion and diffusion imaging we studied the metabolic interplay between supply and demand of nutrients in each compartment. Using multivariate survival analysis, we demonstrate that the volume and lactate level of these two compartments are clinically important.

Results

Multiparametric MRI identifies two low perfusion compartments. A total of 112 patients were included in the study (mean age 59.4 years, range 22-76, 84 males; Overview: Table 1; Study design and patient recruitment: Figure S1). Each patient was imaged using dynamic susceptibility contrast-enhanced (DSC) MRI to measure perfusion, diffusion tensor imaging (DTI) to measure diffusion and ^{1}H magnetic resonance spectroscopy (MRS) chemical shift imaging to measure levels of metabolites. T2-weighted MRI was acquired for anatomical reference. T2-weighted fluid attenuated inversion recovery (FLAIR) images and post-contrast T1-weighted images were acquired to assess the extent of the tumor. The full imaging protocol as well as image post-processing is described in the Methods section. Tumor regions of interest (ROIs) were manually drawn on the post-contrast T1-weighted images and on FLAIR, indicating the solid tumor and the infiltrative regions, respectively. The volumes of each ROI for different patient subgroups is shown and compared in Table 1. As a normal control, ROIs were also drawn on normal-appearing contralateral white matter (NAWM).

Apparent diffusion coefficient (ADC) and relative cerebral blood volume (rCBV) values were obtained from each voxel within the contrast-enhancing (CE) ROI delineated on the post-contrast T1-weighted images (Boonzaier et al., 2017), and low perfusion regions were identified by the lowest quartile of the pooled rCBV values ($rCBV_L$) as shown in Figure 1. The lowest (ADC_L) and highest quartiles (ADC_H) of the ADC maps were overlaid on the $rCBV_L$ maps, defining a tumor compartment with low perfusion and restricted diffusion (ADC_L-$rCBV_L$) and a compartment with low perfusion and high diffusion (ADC_H-$rCBV_L$). Figure 2 (A, D) shows the two compartments for two different tumors. The procedure for identifying these two compartments is illustrated in Figure 1, and Table 1 shows the volume of each compartment for different patient subgroups. The ADC_H-$rCBV_L$ compartment (volume 5.7 ± 4.6 cm^3) was generally larger than the ADC_L-$rCBV_L$ compartment (volume 2.3

± 2.2 cm^3) ($P < 0.001$). Completely resected tumors had smaller CE volume ($P = 0.006$) and smaller ADC_H-$rCBV_L$ compartment ($P = 0.002$). Other regions within the contrast-enhancing ROI but outside the two selected compartments were utilized as abnormal controls (CE control, CEC).

Table 1. Patient clinical characteristics and ROI volumes

Variable	Patient number	CE		FLAIR		ADC_H-$rCBV_L$		ADC_L-$rCBV_L$	
		Mean ± SD (cm^3)	*P*	Mean ± SD (cm^3)	*P*	Mean ± SD (cm^3)	*P*	Mean ± SD (cm^3)	*P*
Age at diagnosis									
<60	38	41.9±24.0	**0.022**	101.4±55.4	0.143	4.3±3.7	**0.020**	1.9±1.6	0.224
≥60	74	58.6±35.7		119.5±63.8		6.3±4.8		2.5±2.4	
Sex									
Male	84	54.5±34.1	0.323	115.2±62.8	0.675	5.8±4.6	0.657	2.4±2.3	0.328
Female	28	48.5±30.0		107.7±57.8		5.4±4.4		1.9±1.8	
Extent of resection									
Complete	75	45.8±26.0	**0.006**	106.0±58.0	0.062	4.8±3.9	**0.002**	2.1±1.8	0.685
Partial	37	67.4±40.8		128.3±66.1		7.5±5.2		2.6±2.8	
MGMT-methylation status*									
Methylated	48	48.4±32.7	0.154	105.4±66.3	0.161	4.8±4.1	0.099	2.2±2.4	0.282
Unmethylated	60	55.8±32.1		121.1±57.9		6.1±4.5		2.4±2.0	
IDH-1 mutation status									
Mutant	7	54.6±35.4	0.895	102.2±69.1	0.471	5.8±4.9	0.843	2.2±1.7	0.787
Wild-type	105	52.9±33.1		114.1±61.2		5.6±4.6		2.3±2.2	

*MGMT-methylation status unavailable for 4 patients. CE: Contrast-enhancing; cm: centimeters; FLAIR: fluid attenuated inversion recovery; ADC_L-$rCBV_L$: region of low-ADC and low-rCBV; ADC_H-$rCBV_L$: region of high-ADC and low-rCBV; IDH-1: Isocitrate dehydrogenase1; MGMT: O-6-methylguanine-DNA methyltransferase; SD: Standard deviation.

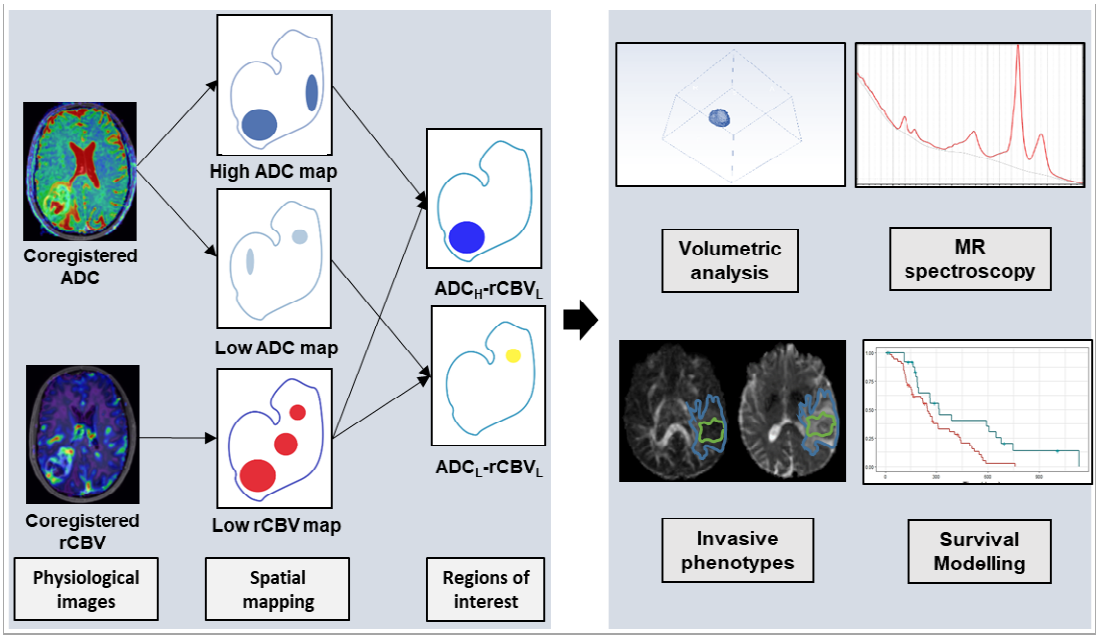

Figure 1. Illustration of the pipeline to identify two ADC-rCBV compartments. Both ADC and rCBV maps are coregistered to the T2 weighted images and tumor regions are segmented manually. Low perfusion tumor regions are partitioned using a quartile threshold. Similarly, two ADC sub-regions are partitioned using high and low ADC quartile thresholds respectively. The spatial overlap between the thresholded rCBV and ADC maps defined two compartments ADC_H-$rCBV_L$ and ADC_L-$rCBV_L$. MR volumetric and metabolic analyses of both compartments are performed and interrogated in invasive tumor phenotype and patient survival analysis models.

Low perfusion compartments displayed hypoxic and pro-inflammatory metabolic signatures. MRS was used to further assess the metabolism in each tumor sub-region for patients with sufficient overlap between the low perfusion regions and the region examined by MRS (we refer to Methods for analysis details). We measured the lactate (Lac) and macromolecule and lipid levels at 0.9 ppm (ML9) in the spectra, as an increase in Lac is frequently detected in hypoxic microenvironments, while ML9 was recently associated with pro-inflammatory microglial response to immune stimulus (Pardon et al., 2016).

The low perfusion and high diffusion compartment ADC_H-$rCBV_L$ showed a significantly higher lactate/creatine (Lac/Cr) ratio than NAWM ($P < 0.001$), as well as an increased ML9/Cr ratio compared to NAWM ($P < 0.001$). Similarly, the ADC_L-$rCBV_L$ compartment displayed higher Lac/Cr ratio and ML9/Cr ratio than NAWM (both $P < 0.001$). Although not significant, the Lac/Cr and ML9/Cr ratios in the ADC_H-$rCBV_L$ compartment

were higher than the ADC_L-$rCBV_L$ compartment (Table S1). Figure 2 shows overlays between the rCBV-ADC compartments and the MRS voxels for two example cases, as well as the metabolite levels in each ROI and compartment.

The contrast-enhancing (CE) tumor volume was significantly correlated with the Lac/Cr ratio in the ADC_L-$rCBV_L$ (P = 0.018, rho = 0.34), indicating that this compartment had higher lactate level in tumors with a larger CE volume. Interestingly, the volume of tumor infiltration beyond contrast enhancement, which was delineated on FLAIR images and normalized by CE volume, showed a moderate positive correlation with the proportional volume of the ADC_L-$rCBV_L$ compartment (P < 0.001, rho = 0.42) and a negative correlation with the proportional volume of the ADC_H-$rCBV_L$ compartment (P < 0.001, rho = -0.32). This indicated that tumors with a large infiltrative volume tended to have smaller ADC_H-$rCBV_L$ and larger ADC_L-$rCBV_L$ compartments. The correlations of ROI volumes are demonstrated in Figure S2.

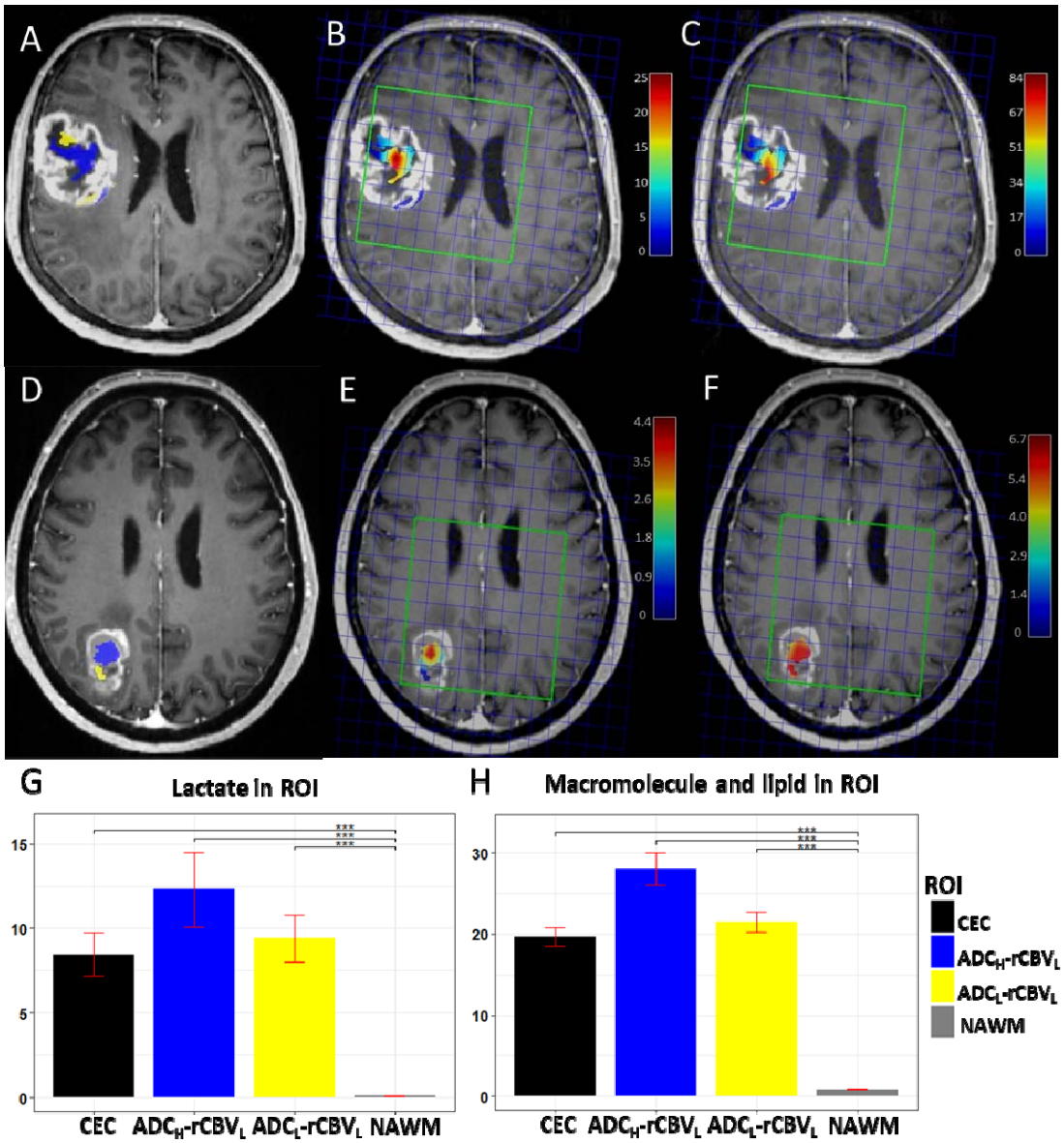

Figure 2. Two hypoxic compartments and MRS characteristics. Case 1: A-C; Case 2: D-F. A & D show the location of ADC_L-$rCBV_L$ (yellow) and ADC_H-$rCBV_L$ (blue) compartments. B & E demonstrate the Lac/Cr ratios of the two compartments. C & F demonstrat the ML9/Cr ratios in the two compartments. The color bar show the level of metabolites (red: high, blue: low). Note that case 1 shows greater tumor volume and higher lactate level. G & H demonstrat the MRS characteristics of the compartments over the patient cohort. Yellow: ADC_L-$rCBV_L$; blue: ADC_H-$rCBV_L$; black: contrast-enhancing control (CEC); grey: normal-appearing white matter (NAWM). G: mean Lac/Cr level; H: mean ML9/Cr. ***: $P < 0.001$.

The low perfusion low diffusion compartment of Minimally invasive tumors is less hypoxic.

To further explore the relation between hypoxic compartments and tumor invasiveness, we investigated diffusion tensor imaging (DTI) based invasive phenotypes of 64 patients overlapping with a previously reported cohort (Price et al., 2017). DTI measures directional diffusion, and is a sensitive method to detect the subtle white matter disruption caused by tumor infiltration (Price et al., 2007). By decomposing the diffusion tensor into isotropic (p) and anisotropic components (q), three invasive phenotypes of glioblastoma have previously been defined (minimal, localized, and diffuse, illustrated in Figure S3), and correlated to patient outcomes and isocitrate dehydrogenase (IDH) mutation status, a prognostic driver mutation of gliomas. The minimally invasive phenotype displayed a lower volume of ADC_L-$rCBV_L$ compartment than the localized (P = 0.031) and diffuse phenotype (not significant), and a higher volume of ADC_H-$rCBV_L$ compartment than the localized (P = 0.024) and diffuse phenotype (not significant), suggesting the contributions of the two low perfusion compartments to tumor invasiveness were different. Of note, the minimally invasive phenotype displayed lower Lac/Cr ratio compared to the localized (P = 0.027) and diffuse phenotype (P = 0.044), indicating that the ADC_L-$rCBV_L$ compartment experienced less hypoxic stress in the minimally invasive tumors. A full comparison between the three invasive phenotypes can be found in Table S2.

Low perfusion compartments exhibited diversity in contribution to treatment response.

We analyzed the available survival data of 80 patients, who received maximal surgery followed by standard regimen of radiotherapy with concomitant temozolomide (TMZ) chemotherapy followed by adjuvant TMZ chemotherapy. The median progression-free

survival (PFS) of these patients was 265 days (range 25-1130 days) and overall survival was 455 days (range 52-1376 days).

First, we used multivariate Cox regression to analyse all the relevant clinical factors. The results showed that extent of resection (EOR) (PFS: hazard ratio [HR] = 2.825, P = 0.003; OS: HR = 2.063, P = 0.024), CE tumor volume (OS: HR = 2.311, P < 0.001) and FLAIR tumor volume (OS: HR = 0.653, P = 0.031) significantly affected survivals.

Next, we included the volumes of two compartments and their weighed average Lac/Cr ratios into the survival models. We used a stepwise procedure to select all prognostic variables. The results showed that higher volumes of the two compartments contributed to better PFS (ADC_H-$rCBV_L$: HR = 0.102, *P* = 0.049; ADC_L-$rCBV_L$: HR = 0.184, *P* = 0.033), whilst the higher Lac/Cr ratio in the two compartments contributed to worse PFS (ADC_H-$rCBV_L$: HR = 6.562, *P* = 0.002; ADC_L-$rCBV_L$: HR = 2.995, *P* = 0.047). Further, the higher Lac/Cr ratio in the ADC_L-$rCBV_L$ compartment also significantly contributed to worse OS (HR = 4.974, *P* = 0.005). In contrast, the Lac/Cr ratio in the contrast-enhancing control regions contributed to better survivals (PFS: HR = 0.053, *P* = 0.001; OS: HR = 0.090, *P* = 0.007). The results of the Cox proportional hazards models are described in Table 2 and the Kaplan-Meier survival curves with log-rank test are shown in Figure 3.

Table 2. Univariate and multivariate modeling of survivals

Factor	PFS						OS					
	Multivariate			Stepwise			Multivariate			Stepwise		
	HR	95%CI	*P*	HR	95%CI	*P*	HR	95%CI	*P*	HR	95%CI	*P*
Age	1.007	0.979-1.035	0.645				1.002	0.971-1.033	0.911	0.927	0.860-0.998	**0.045**
Sex (M)	1.499	0.838-2.681	0.172	5.043	1.063-23.91	**0.042**	1.252	0.662-2.365	0.490			
extent of resection (partial)	2.825	1.417-5.635	**0.003**	4.531	1.002-20.49	**0.050**	2.063	1.099-3.874	**0.024**	12.18	2.701-54.91	**0.001**
MGMT methylation status*	0.624	0.366-1.063	0.083	0.392	0.125-1.233	0.109	0.647	0.358-1.167	0.148	0.231	0.070-0.762	**0.016**
IDH mutation status	0.902	0.278-2.926	0.864				0.900	0.256-3.170	0.870			
CE volume	1.291	0.861-1.935	0.216	6.760	0.696-65.63	0.099	2.311	1.527-3.499	**<0.001**	3.080	1.487-6.383	**0.002**
Flair volume	0.775	0.519-1.157	0.212	2.008	0.818-4.926	0.128	0.653	0.444-0.961	**0.031**			
ADC_L-$rCBV_L$ volume				0.184	0.039-0.874	**0.033**						
ADC_H-$rCBV_L$ volume				0.102	0.011-0.992	**0.049**						
Lac/Cr in ADC_H-$rCBV_L$				6.562	2.023-21.29	**0.002**				2.367	0.825-6.790	0.109
Lac/Cr in ADC_L-$rCBV_L$				2.995	1.012-8.861	**0.047**				4.974	1.608-15.39	**0.005**
Lac/Cr in CEC				0.053	0.010-0.295	**0.001**				0.090	0.016-0.520	**0.007**

*MGMT-methylation status unavailable for 4 patients. PFS: progression-free survival; OS: overall survival; HR: hazard ratio; CI: confidence interval; IDH-1: Isocitrate dehydrogenase1; MGMT: O-6-methylguanine-DNA methyltransferase; CE: Contrast-enhancing; FLAIR: fluid attenuated inversion recovery; Lac: lactate; ADC_L-$rCBV_L$: region of low-ADC and low-rCBV; ADC_H-$rCBV_L$: region of high-ADC and low-rCBV; CEC: contrast enhanced control.

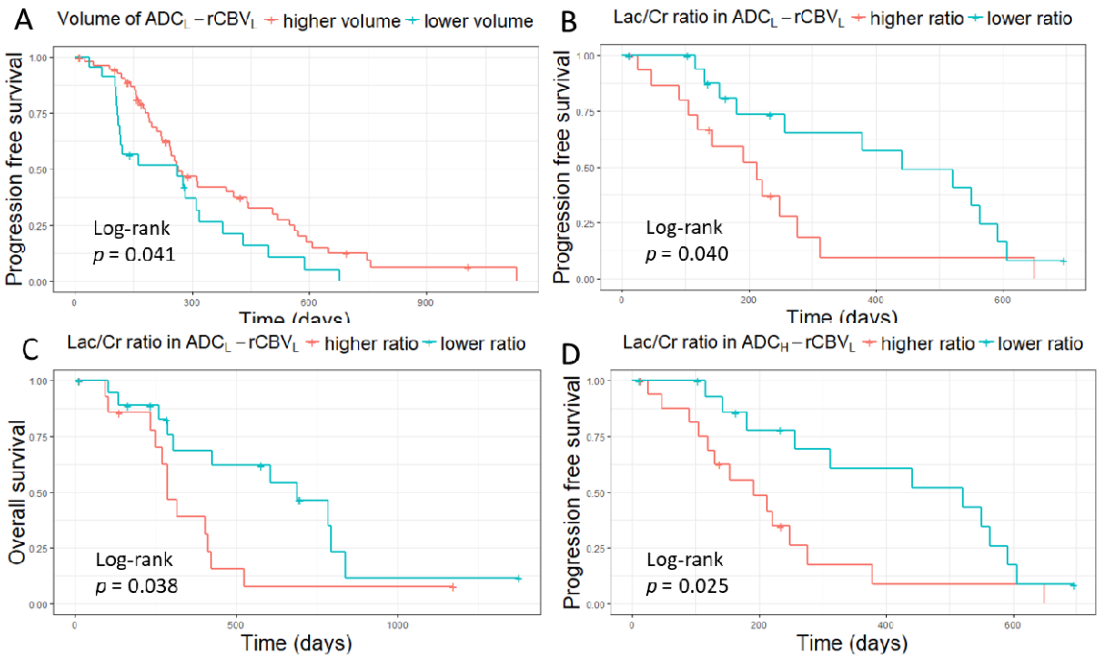

Figure 3. Kaplan-Meier plots of survival analysis. Log-rank tests show larger proportional volume of ADC_L-$rCBV_L$ compartment is associated with better PFS (P = 0.041) (A), while higher Lac/Cr ratio in this compartment is associated with a worse PFS (P =0.040) (B) and OS (P = 0.038) (C). Higher Lac/Cr ratio in the ADC_H-$rCBV_L$ compartment is associated with worse PFS (P = 0.025) (D).

Discussion

This study combined perfusion and diffusion related parameters to define sub-regions of glioblastoma tumors. The two identified low perfusion compartments displayed distinct response to treatment, compared to contrast-enhancing tumor regions. This finding is consistent with recent studies suggesting various adaptive phenotypes exist under selective pressure (Gatenby et al., 2013) and can predict patient survival (Zhou et al., 2016). As far as we know, this is the first study using pretreatment physiological MRI to identify these compartments non-invasively, which may provide crucial information for the determination of tumor invasiveness in clinical decision.

The clinical values of the individual image derived parameters have been extensively assessed previously and are supported by our findings. Among them, rCBV is associated with tumor angiogenesis and proliferation, and has recently been found to indicate IDH mutation status, associated with hypoxia-initiated angiogenesis (Kickingereder et al., 2015). Decreased ADC is thought to represent higher tumor cellularity and cell packing (Chen et al., 2013) and has been associated with shorter survival (Shiroishi, Boxerman, & Pope, 2016). However, it remained unknown if integrating these markers could visualize clinically relevant intratumor habitats. We identified two low perfusion compartments with confirmed hypoxic stress demonstrated by elevated lactate levels compared to normal and abnormal controls. With similar perfusion levels in these two compartments, the higher cellularity (ADC_L) in the ADC_L-$rCBV_L$ compartment suggests that this compartment may display a higher degree of mismatch between supply and demand of nutrients. The elevated ML9/Cr ratios may suggest both compartments displayed elevated inflammation response (Pardon et al., 2016), potentially due to recruitment of tumor-promoting inflammatory cells by necrotic cells (Aktipis, Boddy, Gatenby, Brown, & Maley, 2013; Galluzzi & Kroemer, 2008).

The positive correlation between contrast-enhancing tumor volume and Lac/Cr ratios in the ADC_L-$rCBV_L$ compartment could indicate an acquired hypoxic microenvironment as the solid tumor grows. When evaluating the non-enhancing regions surrounding the solid tumor, we found that tumors with large infiltrative volume tended to have smaller ADC_H-$rCBV_L$ and larger ADC_L-$rCBV_L$ compartments, suggesting that the latter compartment might be more responsible for tumor infiltration. This was supported by our findings that minimally invasive phenotypes displayed significantly lower lactate levels in the ADC_L-$rCBV_L$ compartment.

We further investigated the contributions of the two compartments to patient survivals in a cohort who have received standard dose of concurrent temozolomide (TMZ) chemoradiotherapy followed by adjuvant TMZ after surgery. Interestingly, a higher Lac/Cr ratio in the two compartments was related to worsened outcomes (HR > 1) while this ratio in other contrast-enhancing tumor regions showed a reduced hazard (HR < 1). This suggests that the resistant phenotypes induced by hypoxia mainly nest in the two identified compartments. As the ADC_L-$rCBV_L$ compartment was correlated to tumor infiltration area, diffusion invasiveness, and significantly contributed to both PFS and OS, this compartment may be more responsible for treatment resistance. Additionally, we found that the volumes of both compartments significantly contributed to better survivals in the multivariate model, while the Lac/Cr ratios contributed to worse survivals. These results suggested that the extent of low perfusion, indicated by the volume, and the intensity of hypoxia, indicated by the lactate level, have different clinical implications. Specifically, the higher proportion of the low perfusion compartments may represent a relatively lower proliferative phenotype, while the more intensive hypoxia in these compartment may represent a more aggressive phenotype.

Our findings have clinical significance, as they can help targeting treatment to the selective pressure within tumors. As radiotherapy and chemotherapy can cause selective

stress, our identification of possibly resistant target regions could inform the choice of treatment. Additionally, several recent studies postulated that antiangiogenic agents failed to demonstrate consistent response because they can induce the adaptive clones and thus cause treatment resistance (Hu et al., 2012; Liu et al., 2016). Our findings of the two low perfusion compartments may provide indications for selection of antiangiogenic therapy. Particularly, we suggest more attention might be needed for patients with larger volumes of ADC_L-$rCBV_L$ compartment when considering antiangiogenic agents. The possibility of aggravating hypoxia in this compartment may lead to a more aggressive phenotype.

There are some limitations in our study. While the number of included patients is fairly large, this was a single cohort study. Due to the limited MRS spatial resolution, the multivariate analysis was based on only a subset of the patient cohort. Similarly, the survival analyses were based on the subset of patients who received standard chemoradiotherapy following surgery. The cut-off values defining the two compartments were based on the upper and lower quartiles of the rCBV and ADC distributions, rather than optimizing for threshold specifically. Lastly, although our imaging markers are well validated histologically from other studies (Price et al., 2006), full biological validation can only be achieved with multi-region sampling of each tumor.

In conclusion, we showed that multiparametric imaging could identify two low perfusion compartments displaying heterogeneity in extent and intensity of hypoxia, and consequently exhibiting diversity in tumor invasion and treatment response. The findings in our study may help optimize the current clinical routine which is mainly based on non-specific conventional imaging. The compartment demonstrating both low perfusion and restricted diffusion may indicate a habitat resistant to adjuvant therapies that may aggravate the hypoxic stress. This could provide crucial information for treatment choice in a personalized treatment setting. As our analyses were based on clinically available imaging

modalities, this approach could easily be implemented, and potentially extended to other tumor sites.

Methods

Patient Cohort. A total of 131 patients with a radiological diagnosis of primary supratentorial glioblastoma suitable for maximal safe surgical resection were prospectively recruited from July 2010 to April 2015. Patient recruitment and study design was summarized in Figure S1. Exclusion criteria include history of previous cranial surgery or radiotherapy/chemotherapy, or inability to undergo MRI scanning due to non-MR compatible metallic devices. All patients had a good performance status (World Health Organization performance status 0-1). Preoperative MRI and postoperative histology were performed on all patients. All imaging and histological data were collected prospectively. Patients were all on stable doses (8mg/day) of dexamethasone. Tumor resection was performed with the guidance of neuronavigation (StealthStation, Medtronic) and 5-aminolevulinic acid fluorescence with the maximal safe resection. After surgery, 19 (14.5%) patients were excluded due to non-glioblastoma pathological diagnosis and 112 patients were included. Among them, 82 (73.2%) patients received standard dose of radiotherapy plus temozolomide concomitant and adjuvant chemotherapy post-operatively. Extent of resection was assessed according to the postoperative MRI scans within 72 hours as complete or partial resection of contrast enhancing tumors. Complete resection of contrast enhanced tumor was achieved in 75 of 112 (67.0%) patients and 80 (71.4%) patients had survival data available. Patient survival was analyzed for overall and progression-free survival. The latter was in all follow-up cases made retrospectively to avoid the issue of pseudoprogression. All patients were followed up according to the criteria of response assessment in neuro-oncology (RANO)(Wen et al., 2010). Seven of 112 (6.3%) patients had the IDH-1 R132H mutation and 105 of 112 (93.8%) patients were IDH-1 wild type. MGMT-methylation status was available for 108 patients, among which 48 (44.4%) patients were methylated. This study was approved by local institutional review board, and informed written consent was obtained from all patients.

MRI acquisition. All MRI sequences were performed at a 3-Tesla MRI system (Magnetron Trio; Siemens Healthcare, Erlangen, Germany) with a standard 12-channel receive-head coil. MRI sequences were acquired as following: post-contrast T1-weighted sequence (TR/TE/TI 2300/2.98/900 ms; flip angle 9°; FOV 256 × 240 mm; 176-208 slices; no slice gap; voxel size 1.0 × 1.0 × 1.0 mm) after intravenous injection of 9 mL gadobutrol (Gadovist,1.0 mmol/mL; Bayer, Leverkusen, Germany); T2-weighted sequence (TR/TE 4840-5470/114 ms; refocusing pulse flip angle 150°; FOV 220 × 165 mm; 23-26 slices; 0.5 mm slice gap; voxel size of 0.7 × 0.7 × 5.0 mm); T2-weighted fluid attenuated inversion recovery (FLAIR) (TR/TE/TI 7840-8420/95/2500 ms; refocusing pulse flip angle 150°; FOV 250 × 200 mm; 27 slices; 1 mm slice gap; voxel size of 0.78125 × 0.78125 × 4.0 mm). Perfusion weighted imaging was acquired with a dynamic susceptibility contrast-enhancement (DSC) sequence (TR/TE 1500/30 ms; flip angle 90°; FOV 192 × 192 mm; FOV 192 × 192 mm; 19 slices; slice gap 1.5 mm; voxel size of 2.0 × 2.0 × 5.0 mm;) with 9 mL gadobutrol (Gadovist 1.0 mmol/mL) followed by a 20 mL saline flush administered via a power injector at 5 mL/s. DTI was acquired before contrast enhanced imaging, with a single-shot echo-planar sequence (TR/TE 8300/98 ms; flip angle 90°; FOV 192 × 192 mm; 63 slices; no slice gap; voxel size 2.0 × 2.0 × 2.0 mm). Inline ADC calculation was performed during DTI acquisition from using b values of 0–1000 sec/mm^2. Multivoxel 2D ^{1}H-MRS chemical shift imaging utilized a semi-LASER sequence (TR/TE 2000/30-35 ms; flip angle 90°; FOV 160 × 160 mm; voxel size 10 × 10 × 15-20 mm). PRESS excitation was selected to encompass a grid of 8 rows × 8 columns on T2-weighted images.

Image processing. For each subject, all MRI images were co-registered to T2-weighted images with an affine transformation, using the linear image registration tool (FLIRT)

functions (Jenkinson, Bannister, Brady, & Smith, 2002) in Oxford Centre for Functional MRI of the Brain (FMRIB) Software Library (FSL) v5.0.0 (Oxford, UK) (Smith et al., 2004). DSC data were processed and leakage correction was performed using NordicICE (NordicNeuroLab, Bergen, Norway). The arterial input function was automatically defined and rCBV was calculated in NordicICE. DTI images were processed with a diffusion toolbox (FDT) in FSL (Behrens et al., 2003), during which normalization and eddy current correction were performed. The isotropic component (p) and anisotropic component (q) were calculated using the equation as previously described (Pena et al., 2006). MRS data were processed using LCModel (Provencher, Oakville, Ontario) and the concentrations of lactate (Lac) and macromolecule and lipid levels at 0.9 ppm (ML9) were calculated as a ratio to creatine (Cr). All relevant spectra from MRS voxels of interest were assessed for artefacts using previously published criteria (Price et al., 2016). The values of the Cramer–Rao lower bounds were used to evaluate the quality and reliability of MRS data and values with standard deviation (SD) > 20% were discarded (Price et al., 2016).

Regions of interest and volumetric analysis. Tumor Regions of interest (ROIs) were manually drawn using an open-source software 3D slicer v4.6.2 (https://www.slicer.org/) (Fedorov et al., 2012) by a neurosurgeon with > 7 years of experience (××) and a researcher with > 4 years of brain tumor image analysis experience (××) and reviewed by a neuroradiologist with > 8 years of experience (××) on the post-contrast T1WI and FLAIR. The interrater variability of the ROIs showed good agreement between the two raters, with Dice similarity coefficient scores of 0.85 ± 0.10 (CE) and 0.86 ± 0.10 (FLAIR) respectively. For each individual patient, ROIs of normal-appearing white matter (NAWM) were drawn with the same method in the contralateral white matter as a normal control. All images were

normalized by the mean value in NAWM. Further processing was done using MATLAB (v2016a, The MathWorks, Inc., Natick MA).

Firstly, ADC and rCBV values were obtained from each voxel within the contrast-enhancing (CE) ROI delineated on the post-contrast T1-weighted images and pooled together as described previously (Boonzaier et al., 2017). The lowest quartile of the pooled rCBV values ($rCBV_L$) were interpreted as low perfusion regions. Then the first quartile (ADC_L) and last quartile (ADC_H) of ADC map were respectively overlaid on $rCBV_L$ maps. Finally, two intersections of ADC_L-$rCBV_L$ and ADC_H-$rCBV_L$ ROIs were obtained (Figure 1). Other regions within CE outside the two ADC-rCBV ROIs were taken as abnormal controls (CE control, CEC). Raw volumes of ROIs were calculated using the function of fslmaths in FSL (Smith et al., 2004). Proportional volumes (%) of two ADC-rCBV ROIs were calculated as the ratio of the raw volumes to CE volume.

Multivoxel MRS processing. Due to the difference in spatial resolution between MRS and MRI, voxels from T2-weighted MRIs were projected onto MRS according to their coordinates using MATLAB. Thus, the metabolic status in each voxel could be matched to the voxels in the MRI derived physiological maps, which were coregistered to T2-weighted images. The proportion of T2-space tumor voxels occupying each MRS voxel was calculated, and only those MRS voxels that were completely within the delineated tumor were included in further analyses. The weight of each MRS voxel was taken as the proportion of the ADC-rCBV compartments in that MRS voxel. The weighted sum value was used as final metabolic value of the tumor ROI. This method provides an objective method for MRS voxel selection. The selection criteria for MRS data are demonstrated by Figure 4.

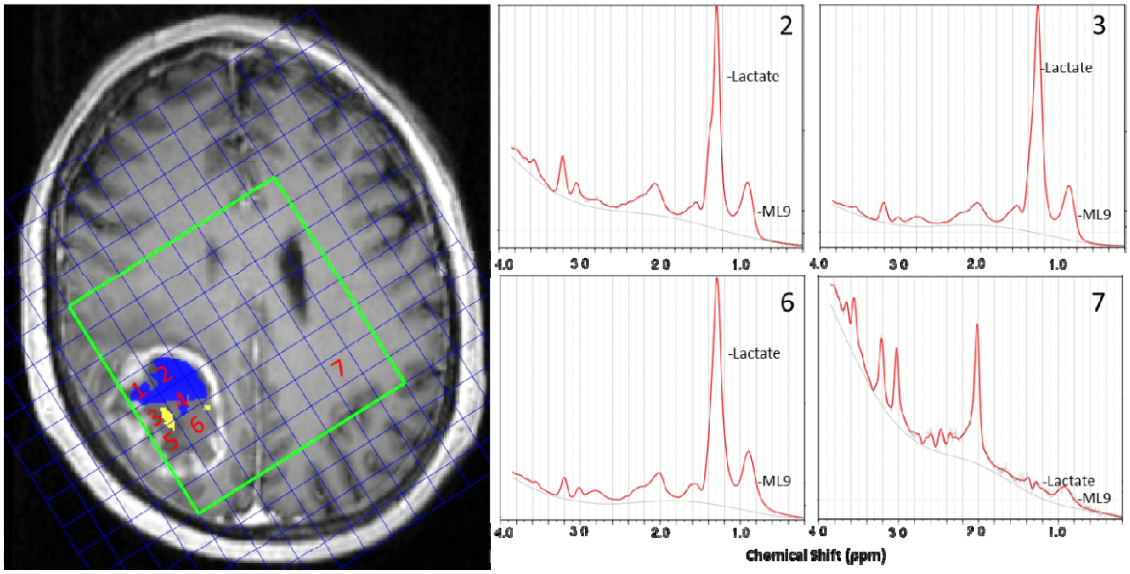

Figure 4. Illustration of multiple voxel MRS analysis. Left: the selection criteria. The T2-space pixels are projected to MRS space according to their coordinates. The proportion of T2-space tumor pixels occupying each MRS voxel is calculated. A criterion is applied that only those MRS voxels are included when this voxel is completely within delineated tumor. In this case, grid 1-6 met the criteria. A weighted average metabolite content for each region is calculated from the metabolite content of each voxel within it weighted by that voxel's percentage of (ADC_H-$rCBV_L$ [blue]: grid 1,2 and 4 are counted; ADC_L-$rCBV_L$ [yellow], grid 3 and 5 are counted; abnormal control [CEC]: grid 1-6 are counted). Right: Example spectra of ROIs. Each spectrum corresponds to the grids on the left. Grid 2: lactate/Cr ratio 13.2, ML9/Cr ratio: 10.4; grid 3: lactate/Cr ratio 28.4, ML9/Cr ratio: 22.7; grid 6: lactate/Cr ratio 8.9, ML9/Cr ratio: 16.6; grid 7 (NAWM): lactate/Cr ratio 0.37, ML9:1.36.

Statistical analysis. All analyses were performed with RStudio v3.2.3. Continuous variables were tested with Welch Two Sample t-test. MRS data or tumor volume, were compared with Wilcoxon rank sum test or Kruskal-Wallis rank sum test (multiple comparisons), using Benjamini-Hochberg procedure for controlling the false discovery rate in multiple comparisons. Spearman rank correlation was used to model the relation between the volume of two ADC-rCBV ROIs and the volume of CE and FLAIR ROIs. Kaplan-Meier and Cox proportional hazards regression analyses were performed to evaluate patient survival. For the Kaplan-Meier analysis, the volumes of ROIs and MRS variables were dichotomized for OS and PFS before the log-rank test using optimal cutoff values calculated by the function of 'surv_cutpoint' in R Package "survminer". Patients who were alive at the last known follow-

up were censored. To test the contribution of the intensity of hypoxia (measured by Lac/Cr ratio) to patient survival, multivariate Cox regression with forward and backward stepwise procedures was performed for the selection of prognostic variables. The forward procedure initiated from the model which only contained one covariate. The backward procedure initiated from the model in which all covariates were included. For each step, the model obtained after adding or deleting one covariate was evaluated using the Akaike Information Criterion (AIC). The final multivariate Cox regression model was constructed using only the features selected by the stepwise procedures. Significance was accepted at a two-sided significance level of alpha < 0.05.

References

Aktipis, C. A., Boddy, A. M., Gatenby, R. A., Brown, J. S., & Maley, C. C. (2013). Life history trade-offs in cancer evolution. *Nature Reviews Cancer, 13*(12), 883-892. doi:10.1038/nrc3606

Behrens, T. E. J., Woolrich, M. W., Jenkinson, M., Johansen-Berg, H., Nunes, R. G., Clare, S., . . . Smith, S. M. (2003). Characterization and propagation of uncertainty in diffusion-weighted MR imaging. *Magnetic Resonance in Medicine, 50*(5), 1077-1088. doi:10.1002/mrm.10609

Boonzaier, N. R., Larkin, T. J., Matys, T., van der Hoorn, A., Yan, J. L., & Price, S. J. (2017). Multiparametric MR Imaging of Diffusion and Perfusion in Contrast-enhancing and Nonenhancing Components in Patients with Glioblastoma. *Radiology*, 160150. doi:10.1148/radiol.2017160150

Chen, L. H., Liu, M., Bao, J., Xia, Y. B., Zhang, J. Q., Zhang, L., . . . Wang, J. (2013). The Correlation between Apparent Diffusion Coefficient and Tumor Cellularity in Patients: A Meta-Analysis. *Plos One, 8*(11). doi:ARTN e79008
10.1371/journal.pone.0079008

Chinot, O. L., Wick, W., Mason, W., Henriksson, R., Saran, F., Nishikawa, R., . . . Cloughesy, T. (2014). Bevacizumab plus Radiotherapy-Temozolomide for Newly Diagnosed Glioblastoma. *New England Journal of Medicine, 370*(8), 709-722. doi:10.1056/NEJMoa1308345

Fedorov, A., Beichel, R., Kalpathy-Cramer, J., Finet, J., Fillion-Robin, J. C., Pujol, S., . . . Kikinis, R. (2012). 3D Slicer as an image computing platform for the Quantitative Imaging Network. *Magnetic Resonance Imaging, 30*(9), 1323-1341. doi:10.1016/j.mri.2012.05.001

Galluzzi, L., & Kroemer, G. (2008). Necroptosis: A Specialized Pathway of Programmed Necrosis. *Cell, 135*(7), 1161-1163. doi:10.1016/j.cell.2008.12.004

Gatenby, R. A., Grove, O., & Gillies, R. J. (2013). Quantitative imaging in cancer evolution and ecology. *Radiology, 269*(1), 8-15. doi:10.1148/radiol.13122697

Gillies, R. J., Schornack, P. A., Secomb, T. W., & Raghunand, N. (1999). Causes and effects of heterogeneous perfusion in tumors. *Neoplasia, 1*(3), 197-207.

Hanahan, D., & Weinberg, R. A. (2011). Hallmarks of cancer: the next generation. *Cell, 144*(5), 646-674. doi:10.1016/j.cell.2011.02.013

Hu, Y. L., DeLay, M., Jahangiri, A., Molinaro, A. M., Rose, S. D., Carbonell, W. S., & Aghi, M. K. (2012). Hypoxia-Induced Autophagy Promotes Tumor Cell Survival and Adaptation to Antiangiogenic Treatment in Glioblastoma. *Cancer Research, 72*(7), 1773-1783. doi:10.1158/0008-5472.Can-11-3831

Jenkinson, M., Bannister, P., Brady, M., & Smith, S. (2002). Improved optimization for the robust and accurate linear registration and motion correction of brain images. *Neuroimage, 17*(2), 825-841. doi:10.1006/nimg.2002.1132

Kickingereder, P., Sahm, F., Radbruch, A., Wick, W., Heiland, S., von Deimling, A., . . . Wiestler, B. (2015). IDH mutation status is associated with a distinct hypoxia/angiogenesis transcriptome signature which is non-invasively predictable with rCBV imaging in human glioma. *Scientific Reports, 5*. doi:ARTN 16238
10.1038/srep16238

Komar, G., Kauhanen, S., Liukko, K., Seppanen, M., Kajander, S., Ovaska, J., . . . Minn, H. (2009). Decreased blood flow with increased metabolic activity: a novel sign of pancreatic tumor aggressiveness. *Clinical Cancer Research, 15*(17), 5511-5517. doi:10.1158/1078-0432.CCR-09-0414

Lathia, J. D., Heddleston, J. M., Venere, M., & Rich, J. N. (2011). Deadly teamwork: neural cancer stem cells and the tumor microenvironment. *Cell Stem Cell, 8*(5), 482-485. doi:10.1016/j.stem.2011.04.013

Liu, T. T., Achrol, A. S., Mitchell, L. A., Rodriguez, S. A., Feroze, A., Michael, I., . . . Rubin, D. L. (2016). Magnetic resonance perfusion image features uncover an angiogenic

subgroup of glioblastoma patients with poor survival and better response to antiangiogenic treatment. *Neuro Oncol*. doi:10.1093/neuonc/now270

O'Connor, J. P. B., Rose, C. J., Waterton, J. C., Carano, R. A. D., Parker, G. J. M., & Jackson, A. (2015). Imaging Intratumor Heterogeneity: Role in Therapy Response, Resistance, and Clinical Outcome. *Clinical Cancer Research, 21*(2), 249-257. doi:10.1158/1078-0432.Ccr-14-0990

Pardon, M. C., Yanez Lopez, M., Yuchun, D., Marjanska, M., Prior, M., Brignell, C., . . . Faas, H. M. (2016). Magnetic Resonance Spectroscopy discriminates the response to microglial stimulation of wild type and Alzheimer's disease models. *Sci Rep, 6*, 19880. doi:10.1038/srep19880

Pena, A., Green, H. A. L., Carpenter, T. A., Price, S. J., Pickard, J. D., & Gillard, J. H. (2006). Enhanced visualization and quantification of magnetic resonance diffusion tensor imaging using the p : q tensor decomposition. *British Journal of Radiology, 79*(938), 101-109. doi:10.1259/bjr/24908512

Pistollato, F., Abbadi, S., Rampazzo, E., Persano, L., Della Puppa, A., Frasson, C., . . . Basso, G. (2010). Intratumoral Hypoxic Gradient Drives Stem Cells Distribution and MGMT Expression in Glioblastoma. *Stem Cells, 28*(5), 851-862. doi:10.1002/stem.415

Price, S. J., Allinson, K., Liu, H., Boonzaier, N. R., Yan, J. L., Lupson, V. C., & Larkin, T. J. (2017). Less Invasive Phenotype Found in Isocitrate Dehydrogenase-mutated Glioblastomas than in Isocitrate Dehydrogenase Wild-Type Glioblastomas: A Diffusion-Tensor Imaging Study. *Radiology, 283*(1), 215-221. doi:10.1148/radiol.2016152679

Price, S. J., Jena, R., Burnet, N. G., Carpenter, T. A., Pickard, J. D., & Gillard, J. H. (2007). Predicting patterns of glioma recurrence using diffusion tensor imaging. *European Radiology, 17*(7), 1675-1684. doi:10.1007/s00330-006-0561-2

Price, S. J., Jena, R., Burnet, N. G., Hutchinson, P. J., Dean, A. F., Pena, A., . . . Gillard, J. H. (2006). Improved delineation of glioma margins and regions of infiltration with the use of diffusion tensor imaging: An image-guided biopsy study. *American Journal of Neuroradiology, 27*(9), 1969-1974.

Price, S. J., Young, A. M. H., Scotton, W. J., Ching, J., Mohsen, L. A., Boonzaier, N. R., . . . Larkin, T. J. (2016). Multimodal MRI Can Identify Perfusion and Metabolic Changes in the Invasive Margin of Glioblastomas. *Journal of Magnetic Resonance Imaging, 43*(2), 487-494. doi:10.1002/jmri.24996

Quail, D. F., & Joyce, J. A. (2013). Microenvironmental regulation of tumor progression and metastasis. *Nat Med, 19*(11), 1423-1437. doi:10.1038/nm.3394

Shiroishi, M. S., Boxerman, J. L., & Pope, W. B. (2016). Physiologic MRI for assessment of response to therapy and prognosis in glioblastoma. *Neuro Oncol, 18*(4), 467-478. doi:10.1093/neuonc/nov179

Smith, S. M., Jenkinson, M., Woolrich, M. W., Beckmann, C. F., Behrens, T. E. J., Johansen-Berg, H., . . . Matthews, P. M. (2004). Advances in functional and structural MR image analysis and implementation as FSL. *Neuroimage, 23*, S208-S219. doi:10.1016/j.neuroimage.2004.07.051

Sottoriva, A., Spiteri, I., Piccirillo, S. G., Touloumis, A., Collins, V. P., Marioni, J. C., . . . Tavare, S. (2013). Intratumor heterogeneity in human glioblastoma reflects cancer evolutionary dynamics. *Proc Natl Acad Sci U S A, 110*(10), 4009-4014. doi:10.1073/pnas.1219747110

Stupp, R., Mason, W. P., van den Bent, M. J., Weller, M., Fisher, B., Taphoorn, M. J., . . . National Cancer Institute of Canada Clinical Trials, G. (2005). Radiotherapy plus concomitant and adjuvant temozolomide for glioblastoma. *N Engl J Med, 352*(10), 987-996. doi:10.1056/NEJMoa043330

Verhaak, R. G., Hoadley, K. A., Purdom, E., Wang, V., Qi, Y., Wilkerson, M. D., . . . Cancer Genome Atlas Research, N. (2010). Integrated genomic analysis identifies clinically relevant subtypes of glioblastoma characterized by abnormalities in PDGFRA, IDH1, EGFR, and NF1. *Cancer Cell, 17*(1), 98-110. doi:10.1016/j.ccr.2009.12.020

Weller, M., van den Bent, M., Tonn, J. C., Stupp, R., Preusser, M., Cohen-Jonathan-Moyal, E., . . . European Association for Neuro-Oncology Task Force on, G. (2017). European Association for Neuro-Oncology (EANO) guideline on the diagnosis and treatment of adult astrocytic and oligodendroglial gliomas. *Lancet Oncology*. doi:10.1016/S1470-2045(17)30194-8

Wen, P. Y., Macdonald, D. R., Reardon, D. A., Cloughesy, T. F., Sorensen, A. G., Galanis, E., . . . Chang, S. M. (2010). Updated response assessment criteria for high-grade gliomas: response assessment in neuro-oncology working group. *Journal of Clinical Oncology, 28*(11), 1963-1972. doi:10.1200/JCO.2009.26.3541

Zhou, M., Chaudhury, B., Hall, L. O., Goldgof, D. B., Gillies, R. J., & Gatenby, R. A. (2016). Identifying spatial imaging biomarkers of glioblastoma multiforme for survival group prediction. *Journal of Magnetic Resonance Imaging*. doi:10.1002/jmri.25497